

# Waterlike anomalies in hard core–soft shell nanoparticles using an effective potential approach: Pinned vs adsorbed polymers

Cite as: J. Appl. Phys. **127**, 054701 (2020); <https://doi.org/10.1063/1.5128938>

Submitted: 23 September 2019 . Accepted: 20 January 2020 . Published Online: 04 February 2020

Murilo S. Marques , Thiago P. O. Nogueira, Rodrigo F. Dillenburg, Marcia C. Barbosa , and José Rafael Bordin 



View Online



Export Citation



CrossMark

Lock-in Amplifiers  
Find out more today



 Zurich  
Instruments

AIP  
Publishing




# Waterlike anomalies in hard core–soft shell nanoparticles using an effective potential approach: Pinned vs adsorbed polymers

Cite as: J. Appl. Phys. 127, 054701 (2020); doi: 10.1063/1.5128938

Submitted: 23 September 2019 · Accepted: 20 January 2020 ·

Published Online: 4 February 2020



Murilo S. Marques,<sup>1,2,a)</sup>  Thiago P. O. Nogueira,<sup>3</sup> Rodrigo F. Dillenburger,<sup>2</sup> Marcia C. Barbosa,<sup>2</sup>   
and José Rafael Bordin<sup>3,b)</sup> 

## AFFILIATIONS

<sup>1</sup>Centro das Ciências Exatas e das Tecnologias, Campus Reitor Edgard Santos, Universidade Federal do Oeste da Bahia, Rua Bertioga, 892, CEP 47810-059 Barreiras, Bahia, Brazil

<sup>2</sup>Instituto de Física, Universidade Federal do Rio Grande do Sul, Caixa Postal 15051, CEP 91501-970 Porto Alegre, Rio Grande do Sul, Brazil

<sup>3</sup>Departamento de Física, Instituto de Física e Matemática, Universidade Federal de Pelotas, Caixa Postal 354, 96010-900 Pelotas, Rio Grande do Sul, Brazil

**Note:** This paper is part of the Special Topic on Polymer-Grafted Nanoparticles.

<sup>a)</sup>Author to whom correspondence should be addressed: [murilo.sodre@ufob.edu.br](mailto:murilo.sodre@ufob.edu.br)

<sup>b)</sup>[jrbordin@ufpel.edu.br](mailto:jrbordin@ufpel.edu.br)

## ABSTRACT

In this work, a two dimensional system of polymer-grafted nanoparticles is analyzed using large-scale Langevin dynamics simulations. Effective core-softened potentials were obtained for two cases: one where the polymers are free to rotate around the nanoparticle core and a second where the polymers are fixed, with a 45° angle between them. The use of effective core-softened potentials allows us to explore the complete system phase space. In this way, the  $PT$ ,  $T\rho$ , and  $P\rho$  phase diagrams for each potential were obtained, with all fluid and solid phases. The phase boundaries were defined analyzing the specific heat at constant pressure, system mean square displacement, radial distribution function, and discontinuities in the density–pressure phase diagram. Also, due to the competition in the system, we have observed the presence of waterlike anomalies, such as the temperature of maximum density (TMD)—in addition with a tendency of the TMD to move to lower temperatures (negative slope)—and the diffusion anomaly. Different morphologies (stripes, honeycomb, and amorphous) for each nanoparticle were observed. We observed that for the fixed polymer case, the waterlike anomalies are originated from the competition between the potential characteristic length scales, while for the free to rotate case, the anomalies arise due to a smaller region of stability in the phase diagram, and no competition between the scales was observed.

Published under license by AIP Publishing. <https://doi.org/10.1063/1.5128938>

## I. INTRODUCTION

Coarse-grained (CG) representations of macromolecular liquids have gained widespread interest because of their ability to represent large-scale properties of systems that cannot be investigated by atomistic scale simulations because of their large size and long time scales.<sup>1,2</sup>

Among coarse-grained models, core-softened (CS) potentials (characterized by having two preferred particle–particle separations) have been attracting attention due to their connections with the

anomalous behavior of liquid systems including water. They show a variety of shapes: they can be ramplike<sup>3</sup> or continuous shoulderlike.<sup>4–7</sup> Despite their simplicity, these models originate from the desire of constructing a simple two-body isotropic potential capable of describing the complicated features of systems interacting via anisotropic potentials<sup>8,9</sup> and are able to reproduce waterlike anomalies in a qualitative way if competition exists between two characteristic distances.<sup>10,11</sup> If the energy penalty to the particle moves from one scale to another is higher than the particle kinetic energy, then the

particle will get trapped in one length scale, and there will be no competition. As a consequence, there will be no anomalous behavior. This procedure generates models that are analytically tractable and computationally less expensive than the atomistic models. Moreover, they lead to conclusions that are more universal and are related to families of atomistic systems.<sup>12</sup>

The study of chemical building blocks as amphiphilic molecules, colloids, and nanoparticles has attracted much attention in soft matter physical chemistry in recent years due to their properties of self-assembly.<sup>13–16</sup> When in water solution, these large molecules agglomerate. In order to circumvent this phase separation, one of the most important practical methods for stabilizing colloids is by coating the particle with a polymer layer.<sup>17,18</sup> These polymer-grafted nanoparticles (GNPs), composed of an inorganic core and a grafted layer of polymer chains, possess new intriguing electrical conductivity and optical and viscoelastic properties<sup>19–23</sup> not present in the noncoated system. The generated self-assembled structures have applications in medicine, self-driven molecules, catalysis, photonic crystals, stable emulsions, biomolecules, and self-healing materials.<sup>24</sup> Experiments<sup>25</sup> and simulations<sup>26,27</sup> showed that in the case of spherical colloids, the mechanism behind the formation of these distinct patterns is the presence of competitive interactions. These competing forces can appear from the combination of a short-range attraction of the core and a long-range repulsion<sup>28</sup> of the grafted polymers.<sup>29–34</sup>

The objective of our work is to analyze the structural, thermodynamic, and dynamic behavior of 2D polymer-grafted nanoparticle (NP) systems through effective potentials in light of molecular dynamics. Particularly, we are interested in how the specificity of the grafted polymer structure can affect the macroscopic morphology and dynamical behavior of these systems when absorbed in large surfaces or when assembled in quasi-2D solid–liquid interfaces.<sup>35</sup>

One of the characteristics of grafted nanoparticles is that by adding appropriated reactive groups in their surface, it is possible to design new materials. In particular, polymers can be adsorbed to the nanoparticle core by fully or partially coating the surface. In the case of partially coated, the polymers are free to rotate at the nanoparticle surface. If the polymers are grafted to the surface by a reactive group or by polymerization, they cannot rotate.<sup>36</sup>

Here, we address the question of how the two types of attachments affect the phase behavior of the nanoparticle solution. We adopt two complementary strategies. We model the systems using a CG approach in which the chemical interactions are represented by classical interactions. Based on this CG model, we derive effective potentials for the two cases: polymers are pinned to a reactive group and polymers are grafted to the surface. CG models have been used as a powerful tool to explore rather complex systems.<sup>37,38</sup> Additional simplification of using effective potentials not only allows for exploring the complete pressure vs temperature phase diagram with a low computational cost but is also able to focus on the physical mechanism behind the different degrees of freedom of free and nonfree cases.

The rest of the paper is organized as follows: in Sec. II, we discuss the model and details of the simulation. In Sec. III, the results and main discussions are given. In Sec. IV, the conclusions are listed.

## II. THE MODEL AND SIMULATION DETAILS

Here, we employ two complementary approximations to describe the polymer-grafted nanoparticle phase diagram: a coarse-grained model and an effective core-softened potential.

### A. The coarse-grained (CG) model

We employ a two dimensional coarse-grained model proposed in previous works<sup>37,39,40</sup> to describe polymer-grafted nanoparticle interactions. Each core-shell nanoparticle is composed of a central disk with the diameter  $\sigma_{core}$  and with four linear oligomer attached chains. Each chain consists of three beads with the diameter  $\sigma_{bead}$ , connected by a harmonic bond,

$$U_{bond}(r_{ij}) = k(r_{ij} - \sigma_{bead})^2, \quad (1)$$

with  $k = 5000$  in reduced Lennard-Jones (LJ) units. The bead–bead (bb) interaction is modeled by the standard Lennard-Jones (LJ) potential,

$$U_{bb}(r_{ij}) = 4\epsilon \left[ \left( \frac{\sigma}{r_{ij}} \right)^{12} - \left( \frac{\sigma}{r_{ij}} \right)^6 \right] - U_{LJ}(r_{cut}), \quad (2)$$

where  $r_{cut} = 2.5\sigma_{mon}$  and  $\epsilon = \epsilon_{core}/9.0$ . For the core–core (cc) interaction, a 14–7 LJ potential was used,

$$U_{cc}(r_{ij}) = 4\epsilon_c \left[ \left( \frac{\sigma_{core}}{r_{ij}} \right)^{14} - \left( \frac{\sigma_{core}}{r_{ij}} \right)^7 \right] - U_{cc}(r_{cut}), \quad (3)$$

where  $r_{cut} = 2.5\sigma_{core}$ . Finally, the core–bead (cp) interaction is given by a 13.5–6.5 LJ potential,

$$U_{cp}(r_{ij}) = 4\epsilon_{cp} \left[ \left( \frac{\sigma_{cp}}{r_{ij}} \right)^{13.5} - \left( \frac{\sigma_{cp}}{r_{ij}} \right)^{6.5} \right] - U_{cp}(r_{cut}), \quad (4)$$

where  $\sigma_{cp}$  and  $\epsilon_{cp}$  are obtained by the well-known Lorentz–Berthelot combining rules.

The first bead in the polymer chain is connected to the central core by a rigid bond.<sup>41</sup> Two cases of grafted NPs were considered. In the first one, the polymers are held fixed in the core surface with a separation of  $45^\circ$  by the bend cosine square bond angle potential,

$$U_{bend} = \frac{k_{bend}}{2} [\cos(\phi) - \cos(\phi_0)]^2, \quad (5)$$

with  $k_{bend} = 50$  and  $\phi_0 = \pi/4$ . “ $\phi$ ” is the angle between two linear oligomer attached chains (the stretched polymer case) or the angle between two consecutive beads both in contact with the nanoparticle (the curved polymer case); its vertex is the nanoparticle’s center. In the second case, no bending potential was applied, and the polymers are free to rotate around the central colloid. Both structures are illustrated in Fig. 1.

In order to simulate a small silica core, we use in this work  $\sigma_{core} = 1.4$  nm and  $\epsilon_{core}/k_b = 10179$  K, as proposed by Lafitte and coauthors.<sup>37</sup> The polymer beads have a diameter of  $\sigma_{bead} = 0.4$  nm and  $\epsilon_{bead} = \epsilon_{core}/9.0$  and correspond to an ethoxy repeat unit.<sup>40</sup>

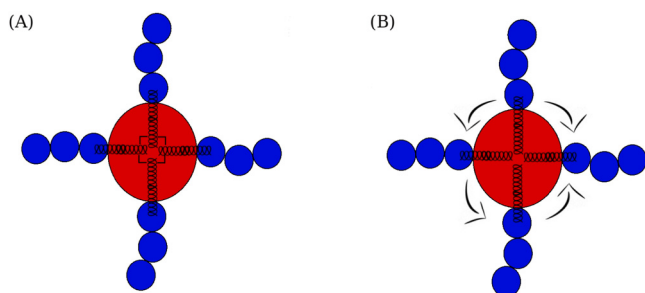


**FIG. 1.** Schematic depiction of the CG nanoparticles. (a) Nanoparticles with a bend potential that prevent the polymers to slide along the core surface and (b) nanoparticles without a bend potential whose polymers are free to rotate along the core surface.

For simplicity, from now on, all the physical quantities in this paper will be displayed in the standard LJ units. Distance, density of particles, time, pressure, and temperature are given, respectively, by

$$\begin{aligned} r^* &\equiv \frac{r}{\sigma_{core}}, & \rho^* &\equiv \rho \sigma_{core}^3, & t^* &\equiv t \left( \frac{\epsilon_{core}}{m \sigma_{core}^2} \right)^{1/2}, \\ p^* &\equiv \frac{\rho \sigma_{core}^3}{\epsilon_{core}}, & \text{and } T^* &\equiv \frac{k_B T}{\epsilon_{core}}. \end{aligned} \quad (6)$$

### B. The effective core-softened potential

The effective core-softened (CS) potentials for the two polymer-grafted nanoparticle systems analyzed here were obtained as follows. Langevin dynamics simulations using the ESPResSo package<sup>42,43</sup> were performed for the coarse-grained models (fixed and free beads). The Langevin dynamics included local hydrodynamics effects in the system.<sup>44</sup> A drag force,  $-\gamma \vec{v}_i$ , with a damping parameter  $\gamma = 1.0$ , acts in each  $i$ th particle and is proportional to the particle velocity  $\vec{v}_i$ , and a random white noise acts as the Brownian force to mimic the collisions with the implicit solvent. As obtained from the fluctuation-dissipation theorem, this force is  $\sqrt{2\gamma k_B T} R(t)$ , where  $k_B$  is the Boltzmann constant,  $T$  is the system temperature, and  $R(t)$  is a delta-correlated stationary Gaussian process with a zero mean. Once the system is in an equilibrium state, we do not expect that long-range hydrodynamic effects should be relevant. The two systems were analyzed in the  $NVT$  ensemble for a density of  $\rho^* = 0.25$  and a temperature of  $T^* = 0.5$ . These values were chosen to ensure that the coarse-grained models were both in the fluid state.

Then, the core-core radial distribution functions (RDFs) for this state point for each fixed and free bead systems were computed, as illustrated in Fig. 2. As we can see, the RDFs indicate a significant difference in the length scale occupancy. For the case of fixed polymers, the black curve in Fig. 2, it is harder for the cores to remain close to each other. As a consequence, this NP has a higher occupancy in the second length scale (the polymer corona) and a smaller in the first length scale—the hard core. The opposite is observed in the red curve of Fig. 2, corresponding to NP with the polymers free to rotate, where the cores can approximate easily,

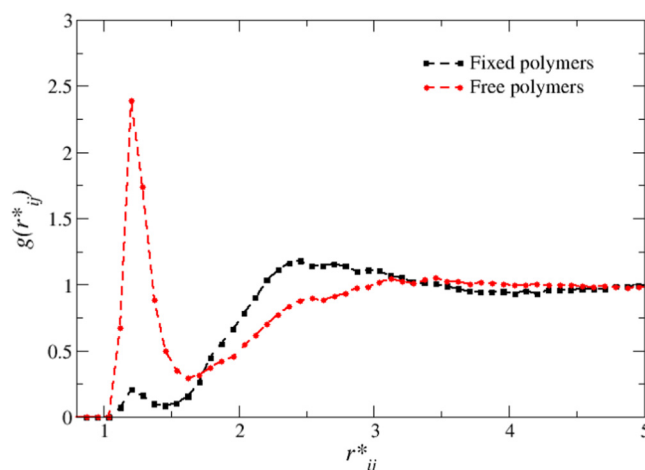


**FIG. 2.** Radial distribution functions employed to obtain the effective interaction potential between NPs with polymers fixed (black squares) or free (red circles) to rotate. Both RDFs were obtained at a density of  $\rho^* = 0.25$  and a temperature of  $T^* = 0.5$ .

increasing the occupancy in the first length scale and decreasing in the second length scale.

From these RDF curves, using the solution of the Ornstein-Zernike (OZ) equation with the integral equation approximation, the effective potentials for polymer-grafted nanoparticles with fixed and free beads were obtained.<sup>37,45,46</sup> To state briefly, the OZ equation,

$$h(r) = c(r) + \rho \int c(\mathbf{r} - \mathbf{r}') h(\mathbf{r}') d\mathbf{r}', \quad (7)$$

averaged over the orientational degrees of freedom, can lead to an exact relation between the translationally invariant radial distribution function,  $h(r) = g(r) - 1$ ; the direct correlation function,  $c(r)$ ; and the system density  $\rho$ .<sup>45</sup> To obtain proper relations between the effective potential and pair correlation functions, an appropriate closure has to be chosen. Here, the hypernetted chain (HNC) approximation was employed for the closure. The potentials were also obtained using the inverse-Boltzmann procedure.<sup>47</sup> In this method, the

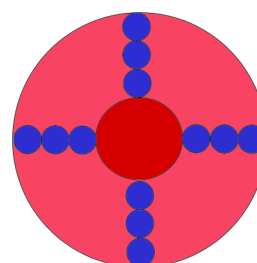


**FIG. 3.** Schematic depiction of the effective nanoparticles. It has a central hard core (the red sphere) and a soft corona (the lighter red sphere).

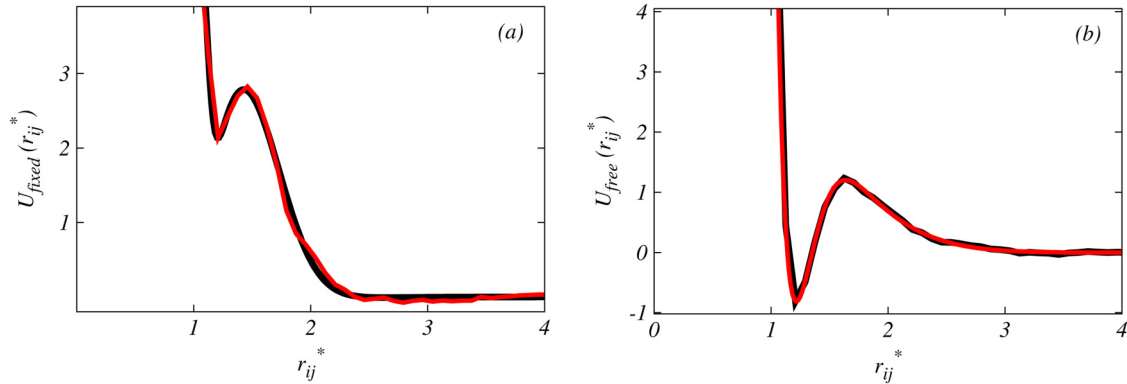


**FIG. 4.** Core-softened potential for polymer-grafted nanoparticles with four monomers (a) fixed and (b) free to rotate around the nanoparticle core. The red curve is the potential obtained by solving the Ornstein-Zernike equation, and the black curve is the LJ plus Gaussian fit.

effective pair interaction  $U_{eff}$  is iteratively updated to match the pair correlation functions of a targeting system,

$$U_{eff}^{i+1} = U_{eff}^i + k_B T \ln \left( \frac{g^i(r)}{g^{target}(r)} \right). \quad (8)$$

Here,  $g^{target}(r)$  is the core-core RDF obtained from the CG simulations and  $g^i(r)$  is the RDF obtained in the  $i$ th iteration. 50 iterations were sufficient to obtain the convergence. Essentially, the same potentials were obtained by both methods.

The polymer-grafted nanoparticles are represented by spherical particles interacting through these effective core-softened potentials, as illustrated in Fig. 3.

Based on previous works,<sup>6,45,46</sup> our effective potentials are composed by a short-range attractive Lennard-Jones potential and three Gaussian terms, each one centered in  $c_j$ , with depth  $h_j$  and width  $w_j$ ,

$$U(r_{ij}) = 4\epsilon_{core} \left[ \left( \frac{\sigma_{core}}{r_{ij}} \right)^{12} - \left( \frac{\sigma_{core}}{r_{ij}} \right)^6 \right] + \sum_{j=1}^3 h_j \exp \left[ - \left( \frac{r_{ij} - c_j}{w_j} \right)^2 \right]. \quad (9)$$

Here,  $r_{ij} = |\vec{r}_i - \vec{r}_j|$  is the distance between two cores  $i$  and  $j$ . The resulting potentials and fittings are shown in Fig. 4 for the case of NP with polymers fixed ( $U_{fixed}$ ) or free ( $U_{free}$ ) to rotate. The parameters corresponding to each case are given in Table I.

The effect of the mobility of the polymers is also clear in the effective potentials. When they are held fixed, the energetic penalty for two NPs that move from the further (or second) scale to the closer (or first) scale is higher than in the case when the polymers can rotate and expose one core to another. As well, this behavior is a consequence of the model, where the bead-bead potential is not intrinsically repulsive at all distances but has a short-range attraction. As a consequence, the  $U_{fixed}$  potential has a ramplike shape, while the  $U_{free}$  has a short-range attraction and a long-range repulsion (SALR) shape.

### C. Simulation details for the effective potential

The system consists of 800 disks with the diameter  $\sigma = \sigma_{core}$ . Langevin dynamics simulations were performed with a time step of  $\delta t = 0.001$ . Periodic boundary conditions were applied in both directions. We performed  $5 \times 10^5$  steps to equilibrate the system. These steps were then followed by  $2 \times 10^6$  timesteps at the production stage. To ensure that the system was thermalized, the pressure, kinetic, and potential energy were analyzed as a function of time. The velocity-Verlet algorithm was employed to integrate the equations of motion. First, MD simulations in the  $NVE$  ensemble were employed to equilibration, followed by Langevin dynamics simulations with controlled pressure ( $NPT$  ensemble) for the production runs. The pressure was held fixed by the Nosè-Hoover barostat with a damping parameter of  $10\delta t$ . The simulations of the effective model were performed using the Large-scale Atomic/Molecular Massively Parallel Simulator (LAMMPS) package,<sup>48</sup> and the  $PT$ ,  $T\rho$ , and  $P\rho$  phase diagrams for each potential were obtained.

The dynamic anomaly was analyzed by the relation between the mean square displacement (MSD) and time, namely,

$$\langle [r(t) - r(t_0)]^2 \rangle = \langle \Delta r^2(t) \rangle, \quad (10)$$

**TABLE I.** Parameters of the particle-particle potentials in reduced units.

Parameter	$U_{fixed}$ potential	$U_{free}$ potential	
	Value	Parameter	Value
$h_1$	2.1895	$h_1$	-3.800 84
$c_1$	0.8199	$c_1$	1.111 92
$w_1$	0.042	$w_1$	0.313 324
$h_2$	9.624	$h_2$	46.132 4
$c_2$	0.7947	$c_2$	0.774 361
$w_2$	0.7197	$w_2$	0.191 852
$h_3$	-3.8685	$h_3$	6.376 21
$c_3$	1.1684	$c_3$	0.192 937
$w_3$	0.2400	$w_3$	1.236 15

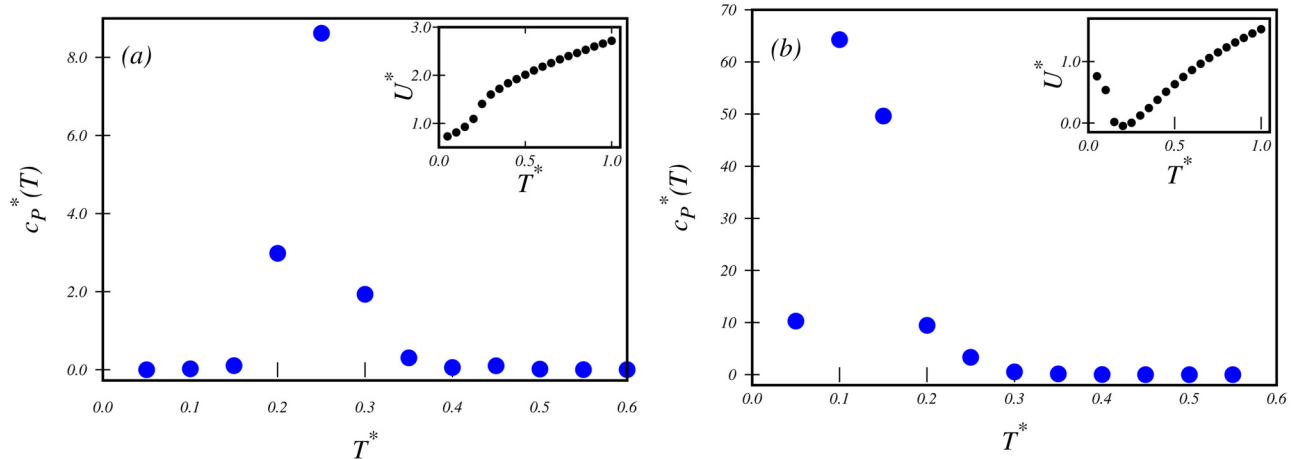


FIG. 5. (a) Specific heat vs temperature at  $P^* = 1.20$  for the  $U_{rigid}$  potential. (b) Specific heat vs temperature at  $P^* = 0.60$  in potential with polymers that are free to rotate. In both, it is possible to see divergences.

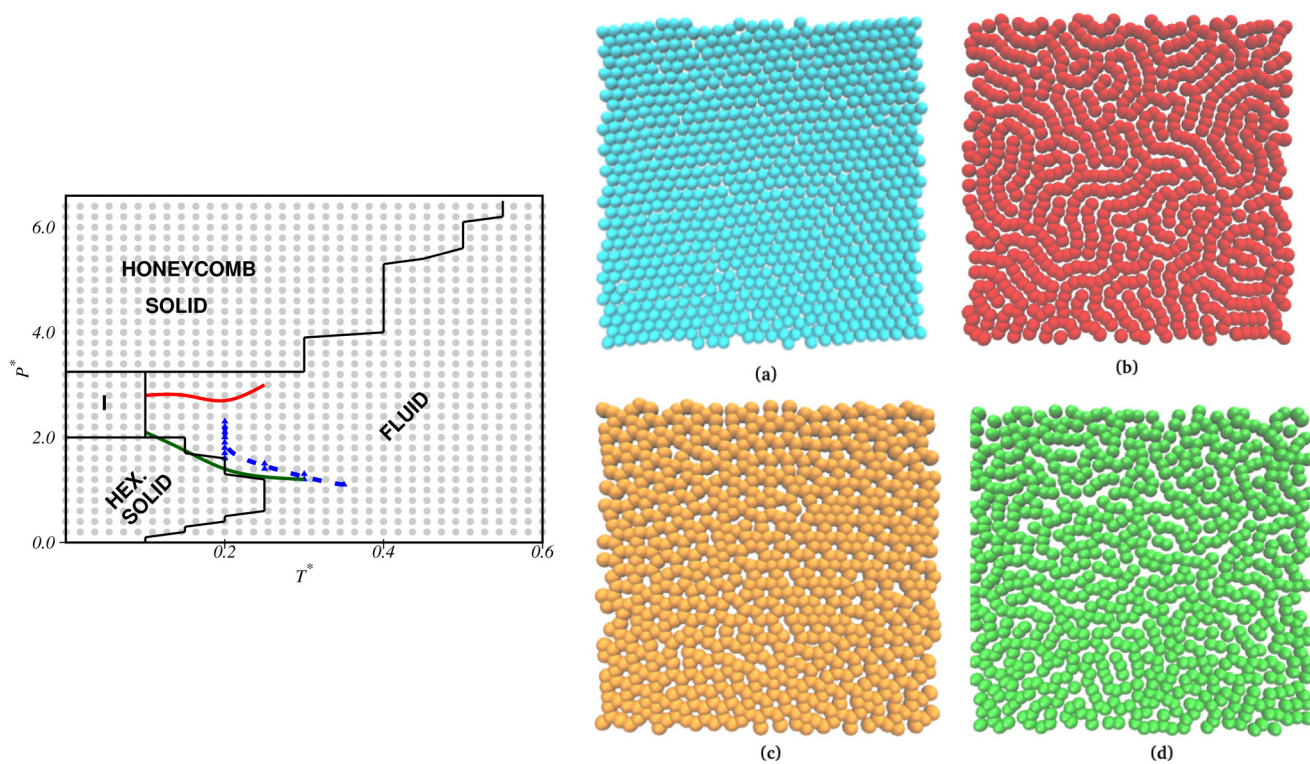


FIG. 6. Left panel: Pressure vs temperature phase diagram of the system with fixed polymers. The gray lines are the isochores, the black lines divide into distinct phases, I represents the hexagonal solid phase, the blue line indicates the TMD, and the green and red lines are the maxima and minima in a diffusion coefficient. Right panel: System snapshots of the (a) hexagonal solid ( $P^* = 0.40$  and  $T^* = 0.05$ ), (b) amorphous solid ( $P^* = 2.80$  and  $T^* = 0.10$ ), (c) honeycomb solid ( $P^* = 5.00$  and  $T^* = 0.20$ ), and (d) fluid ( $P^* = 5.00$  and  $T^* = 0.80$ ).

where  $r(t_0) = (x^2(t_0) + y^2(t_0))^{1/2}$  and  $r(t) = (x^2(t) + y^2(t))^{1/2}$  denote the coordinate of the particle at a time  $t_0$  and at a later time  $t$ , respectively. The MSD is related to the diffusion coefficient  $D$  by Ref. 49,

$$D = \lim_{t \rightarrow \infty} \frac{\langle \Delta r^2(t) \rangle}{4t}. \quad (11)$$

The structure of the fluid was analyzed using the radial distribution function (RDF)  $g(r_{ij})$ . In order to check if the system exhibits the density anomaly, the temperature of maximum density (TMD) was computed for different isobars in the  $T\rho$  diagram.

The phase boundaries here were estimated by analyzing the specific heat at a constant pressure, (Fig. 5),  $C_p$ ,<sup>49</sup> system mean square displacement, radial distribution function, and discontinuities in the density–pressure phase diagram. This approach provides a qualitative depiction of the system melting scenario. Since our focus in this work is the existence of waterlike anomalies, we recommend for the reader the references<sup>50–53</sup> for a more detailed discussion about the three possible melting scenarios in 2D core-softened systems.

### III. RESULTS AND DISCUSSION

Here, we analyze the thermodynamic and dynamic behavior of the system of polymer-grafted nanoparticles represented by the effective core-softened potentials generated for fixed and free bead systems.

#### A. Polymer-grafted nanoparticles with fixed polymers

The pressure vs temperature phase diagram obtained using the effective potential for the grafted nanoparticles with fixed polymers [see the potential in Fig. 4(a)] is illustrated in Fig. 6. Three solid structures were observed. At lower pressures, a hexagonal solid was obtained, as shown in the snapshot [right panel, 6(a)]. Increasing the pressure, the system enters in the region where the anomalous behavior is observed—the waterlike anomalies, which will be discussed next. A consequence of the anomalies in the phase diagram is the presence of a re-entrant liquid phase and a transition from the well-defined hexagonal lattice to an amorphous stripelike structure. This ordered–disordered transition was observed in previous works where particles interact through two length potentials also known as the ramplike potentials.<sup>30,33,54</sup> In the previous works as here, the anomalies arise from the competition between the two length scales. Figure 7 illustrates density vs temperature for a fixed pressure, showing the maximum density, which is a waterlike anomaly.

The effective model is obtained from the coarse-grained system using a radial distribution function for one specific temperature and pressure. This raises the question of how reliable is this approach to describe the system for many pressures and temperatures. In order to test how robust is the effective model, we performed additional simulations for the coarse-grained description of the polymer-grafted colloidal system in the region where the anomalous behavior in the effective model was observed. Then, new  $NPT$  simulations of the CG system were composed of 1000 NPs. Four points in the phase diagram were selected: (I)  $T^* = 0.10$  and  $P^* = 1.0$  (inside the hexagonal solid region of the effective model phase diagram),

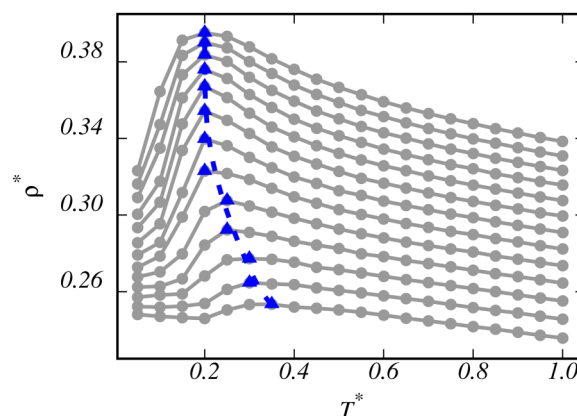


FIG. 7. Temperature of the maxima density for isobars between  $P^* = 1.10$  and  $P^* = 2.30$  from bottom to top.

(II)  $T^* = 0.10$  and  $P^* = 3.0$  (inside the stripe solid region of the effective model phase diagram), (III)  $T^* = 0.10$  and  $P^* = 4.0$  (inside the honeycomb solid region of the effective model phase diagram), and (IV)  $T^* = 0.20$  and  $P^* = 2.0$  (inside the re-entrant fluid phase of the effective model phase diagram). Figure 8 illustrates these state points. The structures are similar to the obtained using the effective model (Fig. 6). This indicates that the effective model was able to capture the proper behavior of the CG model phase diagram.

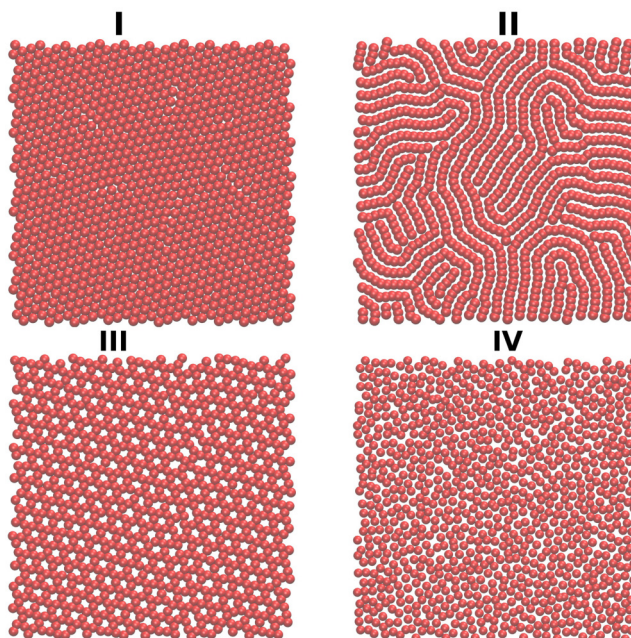


FIG. 8. Comparison between the patterns observed in the CG model and effective model.

One of the characteristics of systems interacting through two length scale potential as the potentials illustrated in Fig. 4 is the presence of thermodynamic anomalies. The density anomaly is characterized by a maximum in the  $\rho(T)$  curve along an isobar. For constant pressure, as the temperature increases, the density increases by making particles to rearrange from one length scale to the other. This can also be observed in the radial distribution function  $g(r_{ij})$ , which presents two peaks: one at the closest scale,  $r_1$ , and another at the furthest scale,  $r_2$ . Recently, it has been suggested that a signature of the presence of the TMD line will be given by the radial distribution function as follows: at fixed temperature, as the density is increased, the radial distribution function of the closest scale,  $g(r_1)$ , will increase its value, while the radial distribution function of the furthest scale,  $g(r_2)$ , will decrease.<sup>55</sup> This can also be represented by the rule,<sup>56,57</sup>

$$\Pi_{12} = \left. \frac{\partial g(r)}{\partial \rho} \right|_{r_1} \times \left. \frac{\partial g(r)}{\partial \rho} \right|_{r_2} < 0. \quad (12)$$

The physical picture behind this condition is that, for a fixed pressure, as the temperature increases, particles that are located at the

attractive scale,  $r_2$ , move to the repulsive scale,  $r_1$ —the thermal effects, which occur up to a certain pressure threshold  $P^*_{\min} = 0.90$ . For pressures in the range  $0.90 < P^* < 3.00$ , for a fixed temperature, as the pressure increases, particles exhibit the same offset between the potential length scales  $r_1$  and  $r_2$ —the pressure effects. Figure 9 illustrates typical radial distribution functions at fixed  $T^*$  as  $P^*$  is varied [(a) and (b)] and vice versa [(c) and (d)].

The regions identified by the radial distribution function fulfilling the condition Eq. (12) are illustrated by red circles in Fig. 11(a). The solid curve shows the TMD line. All the stable state points with the density equal or higher the minimum density at the TMD line verify the relation  $\Pi_{12}(\rho, T) < 0$ . This result gives support to our assumption that the presence of anomalies is related to the particles moving from the furthest scale,  $r_2$ , to the closest length scale  $r_1$ . In addition, it indicates that the two length scales in the effective potential are related to the core-core repulsion competing with the polymer-polymer attraction present in the coarse-grained potential.

Another signature of anomalous fluids is the behavior of the diffusion coefficient, which increases with density. Figure 10

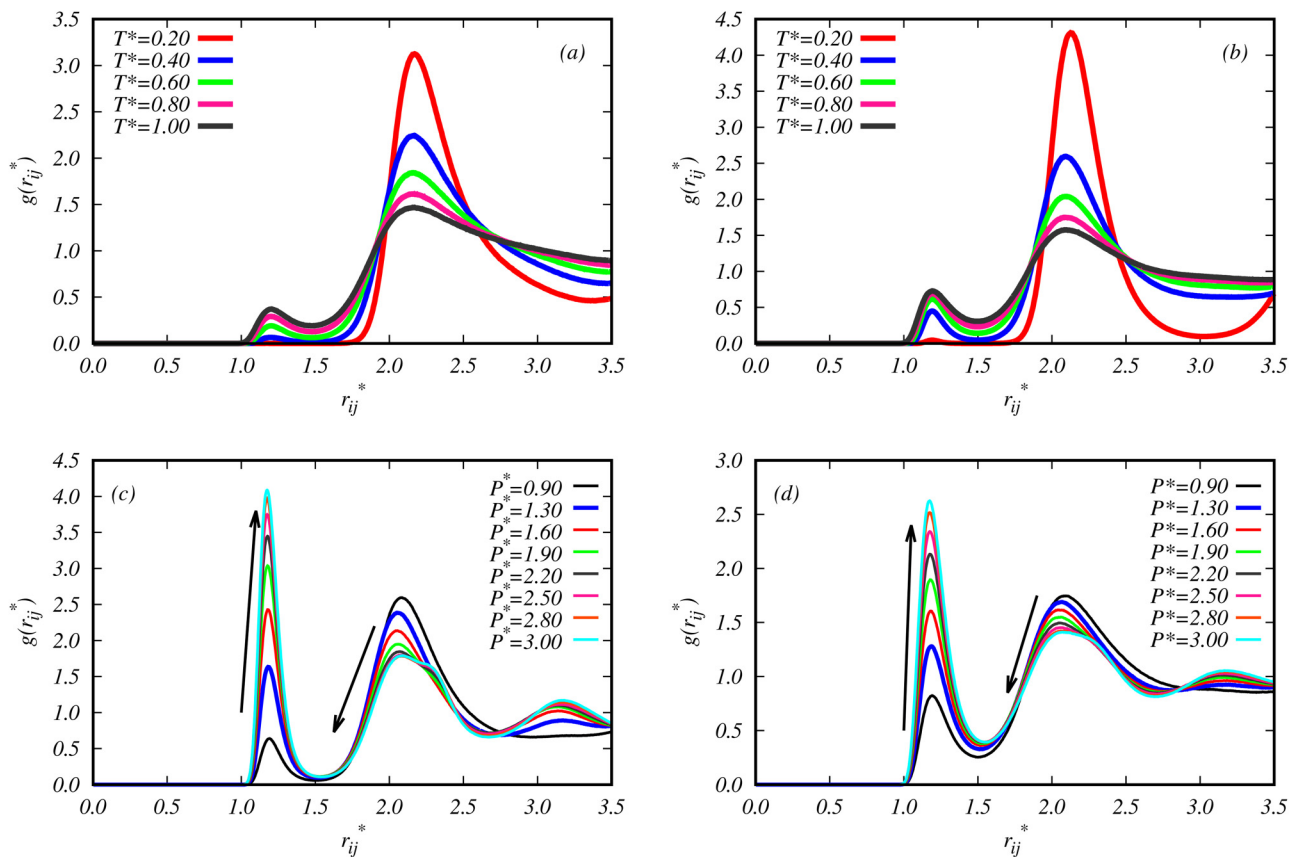


**FIG. 9.** Radial distribution function behavior for pressure two values below the threshold and temperature variation [ $P^* = 0.40$  in (a) and  $P^* = 0.80$  in (b)], indicating thermal effects in this region. Bottom figures: RDFs for two fixed temperatures [ $T^* = 0.40$  in (c) and  $T^* = 0.80$  in (d)] and pressure variation inside the range  $0.90 < P^* < 3.00$ , indicating pressure effects in the TMD region.



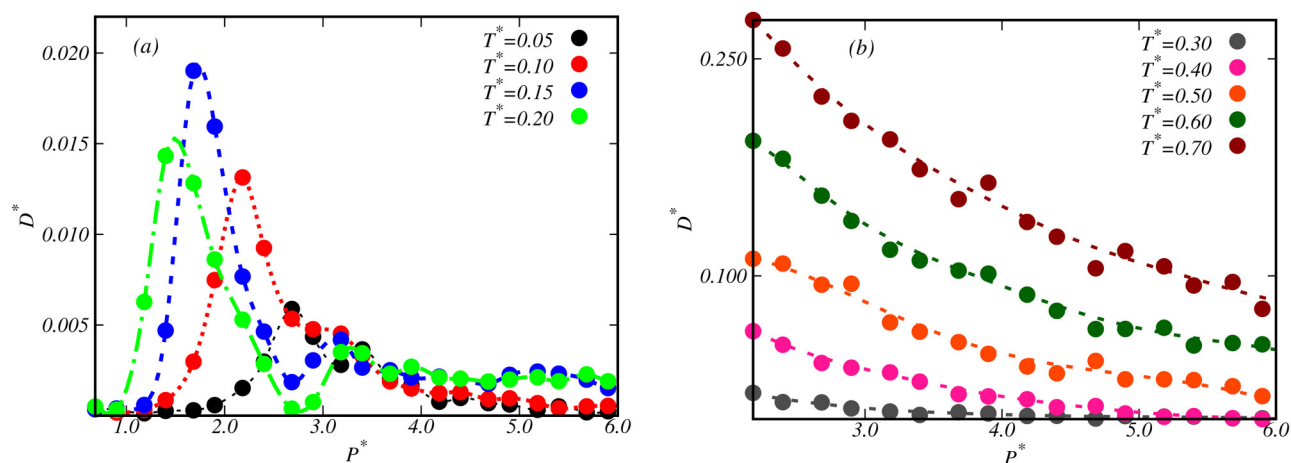


**FIG. 10.** Diffusion coefficient vs pressure for (a)  $T^* = 0.05$  (black line),  $T^* = 0.10$  (red line),  $T^* = 0.15$  (blue line),  $T^* = 0.20$  (green line) and (b)  $T^* = 0.30$  (gray line),  $T^* = 0.40$  (magenta line),  $T^* = 0.50$  (orange line),  $T^* = 0.60$  (green line), and  $T^* = 0.70$  (brown line).

represents the diffusion coefficient vs pressure for different isotherms, showing that  $D$  in a certain range of temperature and pressure increases with pressure. The minimum in the diffusion coincides with the melting line. This behavior of the diffusion and melting line is related to ordered–disordered transition, and it was previously observed for ramplike potentials in two dimensions.<sup>33</sup>

Finally, in order to check if the CG model also shows anomaly, we run simulations along the isobar  $P^* = 2.0$ . Figure 11(b) illustrates the density vs temperature for  $P^* = 2.0$  for both CG (red squares) and effective (black circles) potentials. The two behaviors are quite similar. This result indicates that our strategy to derive simpler two length scale potential to describe a more sophisticated system obtaining some information about the origin of the anomaly is valid.

## B. Polymer-grafted nanoparticles with free nanoparticles

The pressure vs temperature phase diagram obtained using the effective potential for the grafted nanoparticles with free polymers is illustrated in Fig. 12. The phase behavior of the system is quite distinct when compared with the phase diagram for the system with fixed polymers.

At low temperatures ( $T^* \leq 0.10$ ), and for pressures up to  $P^* = 1.40$ , the system is in a hexagonal solid phase. Increasing the temperature for  $P^* < 0.12$ , the system melts to a fluid phase, while in the range  $0.12 < P^* < 1.4$ , there is an ordered–disordered transition in the solid structure, which changes from hexagonal to amorphous.

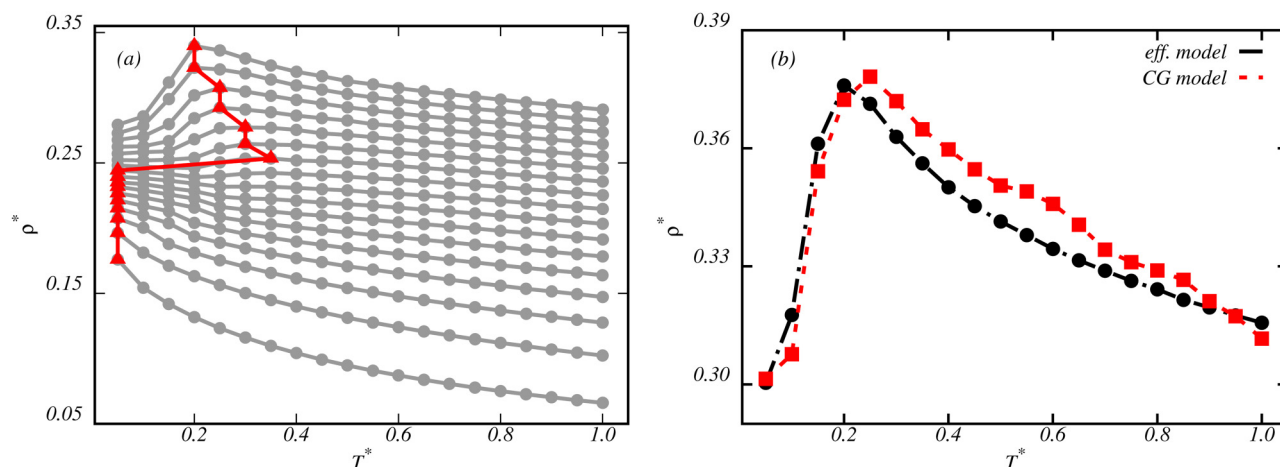


**FIG. 11.** (a) TMD line (red line) for distinct isobars in the effective model. (b) Comparison of one  $\rho(T)$  curve along the isobar  $P^* = 2.0$  between effective (black circles) potentials and the CG model (red squares).

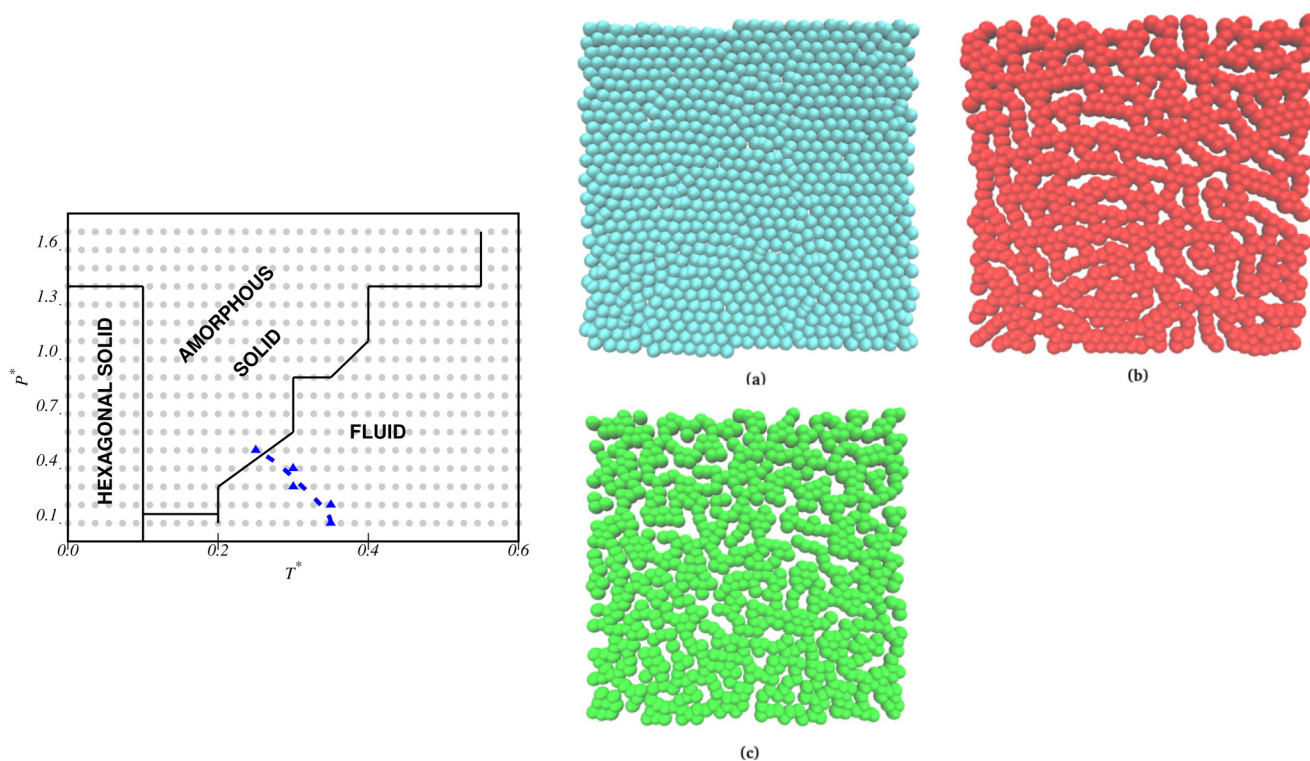


**FIG. 12.** Left panel: Pressure–temperature phase diagram of the system in which polymers are free to rotate. The gray dots are the simulated points. The lines divide into distinct phases, I is the hexagonal phase, II is the amorphous solid, and the blue line is the TMD. Right panel: System snapshots for (a) hexagonal solid ( $P^* = 0.40$  and  $T^* = 0.05$ ), (b) amorphous solid ( $P^* = 1.10$  and  $T^* = 0.10$ ), and (c) fluid ( $P^* = 1.10$  and  $T^* = 0.70$ ).

Both free and fixed polymer systems show a number of similarities in the phase space; here, however, we do not observe a re-entrant fluid phase or the honeycomb solid phase. Also, the solid–liquid separation line moves to higher temperatures. As a

consequence, the TMD line is smaller, and no diffusion anomaly is present.

The absence of the diffusion anomaly when the system exhibits a TMD is not new. It arises in lattice systems in the presence of two

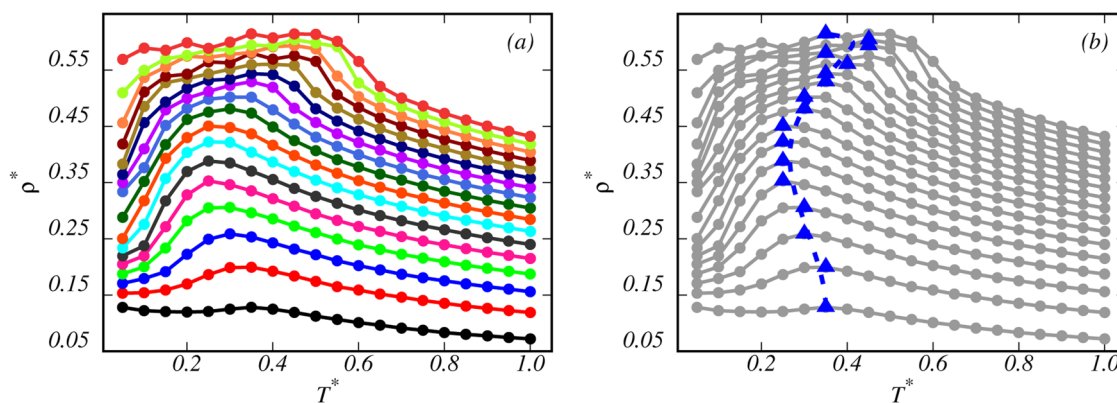


**FIG. 13.** Density–temperature phase diagrams. (a) The color lines are the isobars from  $P^* = 0.10$  (bottom) to  $P^* = 1.70$  (top). (b) The same diagram explaining the maximum density temperature (TMD).

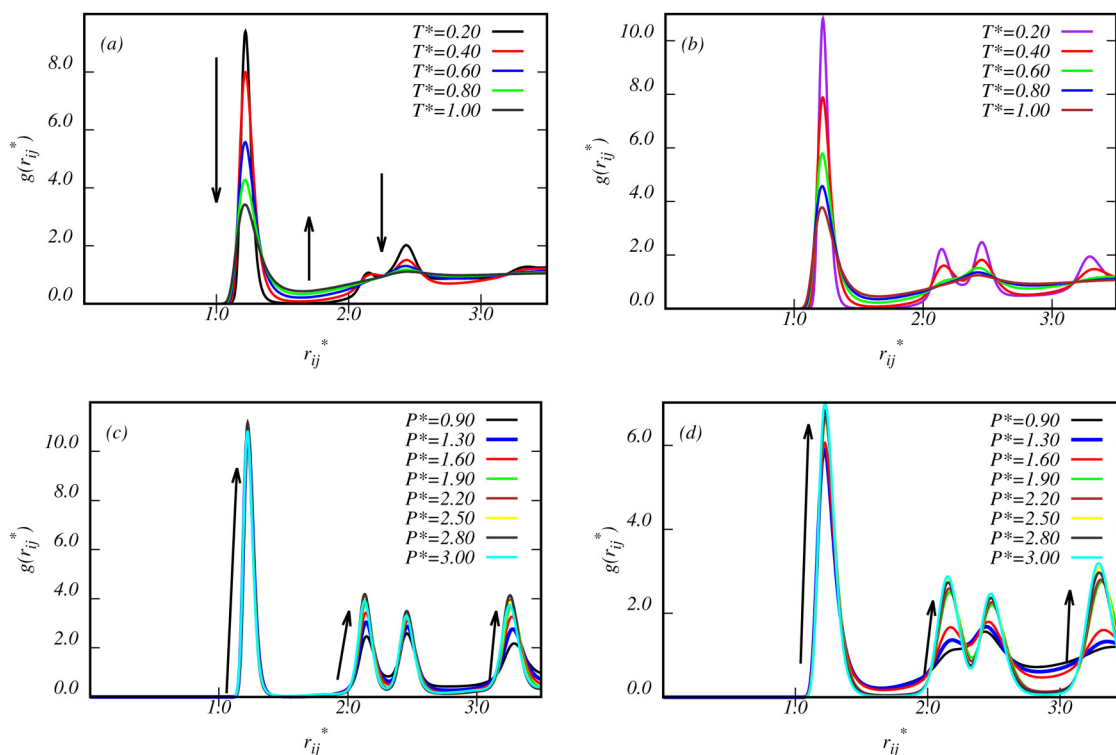


**FIG. 14.** Radial distribution function behavior for maintaining fixed temperature and varying pressure and vice versa in order to verify the relation between competition and structure. (a)  $P^* = 0.40$ , and each curve is from one temperature. (b)  $P^* = 0.80$  analogously. (c)  $T^*$  is fixed at  $T^* = 0.20$ , and pressure is varying. (d)  $T^*$  is fixed at  $T^* = 0.60$ , analogously.

length scale interactions depending on the balance between the two length scales<sup>58</sup> and in confinement due to the competition between the length scales and confinement.<sup>59</sup> In this case, it may be related to the fact that there is no re-entrant fluid region—as we saw here, and these two phenomena were correlated with the  $U_{fixed}$  potential.

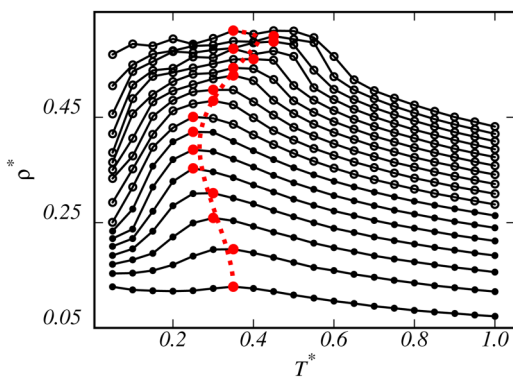


**FIG. 15.** Density–temperature phase diagram confirming its relation between the competition and structure. Filled symbols are dominated by thermal effects, and empty are those dominated by pressure effects.

Usually, the presence of the TMD, as shown in Fig. 13, is related to the competition between the two length scales, as discussed earlier. However, some studies have shown that the same phenomena can occur in fluids without competitive scales, but just weak softening of the interparticle repulsion can lead to anomalous behavior.<sup>60,61</sup>

Therefore, unlike the previous case ( $U_{fixed}$ ), it is not possible to establish the connection between the structure and anomaly by density, as we can see in Fig. 14, which shows behavior of RDFs by varying temperature (at fixed  $P^*$ ) and pressure (at fixed  $T^*$ ). This disconnection can also be analyzed taking into account that the unfilled points of the graph obey the relation between the migration of scales and that, in turn, the TMD reaches all points (filled or not). It is concluded that, for this potential, it will not be the competition between the scales responsible for the density anomaly, as may be seen in Fig. 15. Still, because the potential has a short-range attraction and a long-range repulsion (SALR) shape, it was possible to capture some structural patterns (as a stripe phase) that had already been observed in potentials of two more abrupt scales.<sup>62,63</sup>

#### IV. SUMMARY AND CONCLUSIONS

In this work, a two-dimensional system of polymer-grafted nanoparticles is analyzed using large-scale Langevin dynamics simulations. The use of effective core-softened potentials allow us to

explore the complete system phase space. In this way, the  $PT$ ,  $T\rho$ , and  $P\rho$  phase diagrams for each potential were obtained. The phase boundaries were defined analyzing the specific heat at constant pressure, system mean square displacement, radial distribution function, and discontinuities in the density–pressure phase diagram. Also, due to the competition in the system, we have observed the presence of waterlike anomalies, such as the temperature of maximum density—in addition with a tendency of the TMD to move to lower temperatures (negative slope)—and the diffusion anomaly. Different structural morphologies for each nanoparticle case were observed. We observed that for the fixed polymer case, the waterlike anomalies originated from the competition between the potential characteristic length scales, while for the free to rotate case, the anomalies arise due to a smaller region of stability in the phase diagram, and no competition between the scales was observed.

The main driving force for the different morphologies obtained is the competition between strong short-range attractions of the particle cores (the enthalpic gain upon the core–core aggregation) and long-range entropic repulsions of the grafted chains.

## ACKNOWLEDGMENTS

The authors acknowledge the financial support from the Brazilian agencies FAPERGS and CNPq. T.P.O.N. thanks the Coordenação de Aperfeiçoamento de Pessoal de Nível Superior (CAPES), Finance Code 001, for the financial support. The authors thank Professor Alan Barros de Oliveira from Universidade Federal de Ouro Preto, Minas Gerais, Brazil, and Professor Enrique Lomba from Instituto de Química Física Rocasolano, Madrid, Spain, for facilitating computational time in cluster to run effective model simulations.

## REFERENCES

- 1A. J. Clark, J. McCarty, and M. G. Guenza, *J. Chem. Phys.* **139**, 124906 (2013).
- 2A. Renevey and S. Riniker, *J. Chem. Phys.* **146**, 124131 (2017).
- 3E. A. Jagla, *J. Chem. Phys.* **111**, 8980 (1999).
- 4E. Salcedo, A. B. de Oliveira, N. M. Barraz, C. Chakravarty, and M. C. Barbosa, *J. Chem. Phys.* **135**, 044517 (2011).
- 5Y. D. Fomin, E. N. Tsiok, and V. N. Ryzhov, *J. Chem. Phys.* **135**, 234502 (2011).
- 6N. M. Barraz, E. Salcedo, and M. C. Barbosa, *J. Chem. Phys.* **131**, 094504 (2009).
- 7J. N. da Silva, E. Salcedo, A. B. de Oliveira, and M. C. Barbosa, *J. Chem. Phys.* **133**, 244506 (2010).
- 8G. Birnbaum, *Phenomena Induced by Intermolecular Interactions*, Nato ASI Subseries B (Springer, 2013).
- 9I. Kaplan, *Intermolecular Interactions: Physical Picture, Computational Methods and Model Potentials*, Wiley Series in Theoretical Chemistry (Wiley, 2006).
- 10P. Gallo *et al.*, *Chem. Rev.* **116**, 7463 (2016).
- 11P. Vilaseca and G. Franzese, *J. Non Cryst. Solids* **357**, 419 (2011).
- 12Y. Tsuchiya, *J. Phys. Soc. Jpn.* **60**, 227 (1991).
- 13S. Sacanna, M. Korpics, K. Rodriguez, L. Colón-Meléndez, S.-H. Kim, D. J. Pine, and G.-R. Yi, *Nat. Commun.* **4**, 1688 (2013).
- 14B. T. T. Pham, C. H. Such, and B. S. Hawkett, *Polym. Chem.* **6**, 426 (2015).
- 15Z. Preisler, T. Vissers, F. Smalenburg, G. Munaò, and F. Sciortino, *J. Phys. Chem. B* **117**, 9540 (2013).
- 16A. Kumar and V. Molinero, *J. Phys. Chem. Lett.* **8**, 5053 (2017).
- 17R. Jones, *Soft Condensed Matter*, Oxford Master Series in Physics (OUP, Oxford, 2002).
- 18T. Witten, T. Witten, P. Pincus, P. Pincus, and P. Pincus, *Structured Fluids: Polymers, Colloids, Surfactants* (Oxford University Press, 2004).
- 19A. Chremos and J. F. Douglas, *Soft Matter* **12**, 9527 (2016).
- 20C. Chevigny, F. Dalmas, E. Di Cola, D. Gignes, D. Bertin, F. Boué, and J. Jestin, *Macromolecules* **44**, 122 (2011).
- 21V. Ganesan and A. Jayaraman, *Soft Matter* **10**, 13 (2014).
- 22D. F. Sunday and D. L. Green, *Macromolecules* **48**, 8651 (2015).
- 23D. V. Talapin, J. S. Lee, M. V. Kovalenko, and E. V. Shevchenko, *Chem. Rev.* **110**, 389 (2010).
- 24J. Zhang, E. Luijten, and S. Granick, *Annu. Rev. Phys. Chem.* **66**, 581 (2015).
- 25H. N. Lokupitiya, A. Jones, B. Reid, S. Guldin, and M. Stefiik, *Chem. Mater.* **28**, 1653 (2016).
- 26B. A. Lindquist, S. Dutta, R. B. Jadrich, D. J. Milliron, and T. M. Truskett, *Soft Matter* **13**, 1335 (2017).
- 27D. F. Schwanzler, D. Coslovich, and G. Kahl, *J. Phys. Condens. Matter* **28**, 414015 (2016).
- 28A. Shukla, E. Mylonas, E. Di Cola, S. Finet, P. Timmins, T. Narayanan, and D. I. Svergun, *Proc. Natl. Acad. Sci. U.S.A.* **105**, 5075 (2008).
- 29J. R. Bordin and M. C. Barbosa, *Langmuir* **31**, 8577 (2015).
- 30L. B. Krott, C. Gavazzoni, and J. R. Bordin, *J. Chem. Phys.* **145**, 244906 (2016).
- 31J. R. Bordin, *Physica A* **459**, 1 (2016).
- 32J. R. Bordin, *Physica A* **495**, 215 (2018).
- 33J. R. Bordin and M. C. Barbosa, *Phys. Rev. E* **97**, 022604 (2018).
- 34J. R. Bordin, *Fluid Phase Equilib.* **499**, 112251 (2019).
- 35K. Volk, F. Deisenbeck, S. Mandal, H. Löwen, and M. Karg, *Phys. Chem. Chem. Phys.* **21**, 19153 (2019).
- 36M. J. A. Hore, *Soft Matter* **15**, 1120 (2019).
- 37T. Lafitte, S. K. Kumar, and A. Z. Panagiotopoulos, *Soft Matter* **10**, 786 (2014).
- 38B. Song, N. Charest, H. A. Morriss-Andrews, V. Molinero, and J. Shea, *J. Comp. Chem.* **38**, 1353 (2017).
- 39P. Akcora, H. Liu, S. K. Kumar, Y. L. Joseph Moll, B. C. Benicewicz, L. S. Schadler, D. Acehan, A. Z. Panagiotopoulos, V. Pryamitsyn, V. Ganesan, J. Ilavsky, P. Thiyagarajan, R. H. Colby, and J. F. Douglas, *Nat. Mater.* **8**, 354 (2009).
- 40B. Hong, A. Chremos, and A. Z. Panagiotopoulos, *Faraday Discuss.* **154**, 29 (2012).
- 41J. P. Ryckaert, G. Ciccotti, and H. J. C. Berendsen, *J. Comput. Phys.* **23**, 327 (1977).
- 42H.-J. Limbach, A. Arnold, B. A. Mann, and C. Holm, *Comput. Phys. Commun.* **174**, 704 (2006).
- 43A. Arnold, O. Lenz, S. Kesselheim, R. Weeber, F. Fahrenberger, D. Roehm, P. Kosovan, and C. Holm, “Espresso 3.1: Molecular dynamics software for coarse-grained models,” in *Meshfree Methods for Partial Differential Equations VI*, Lecture Notes in Computational Science and Engineering (Springer, Berlin, 2013), Vol. 89, pp. 1–23.
- 44M. Megnidio-Tchoukouegno, F. Gaiho, G. Mola, M. Tsige, and G. Pellicane, *Fluid Phase Equilib.* **441**, 33 (2017).
- 45T. Head-Gordon and F. H. Stillinger, *J. Chem. Phys.* **98**, 3313 (1992).
- 46Z. Yan, S. V. Buldyrev, P. Kumar, N. Giovambattista, and H. E. Stanley, *Phys. Rev. E* **77**, 042201 (2008).
- 47N. G. Almarza, E. Lomba, and D. Molina, *Phys. Rev. E* **70**, 021203 (2004).
- 48S. Plimpton, *J. Comput. Phys.* **117**, 1 (1995).
- 49M. Allen and D. Tildesley, *Computer Simulation of Liquids: Second Edition* (OUP, Oxford, 2017).
- 50D. E. Dudalov, E. N. Tsiok, Y. D. Fomin, and V. N. Ryzhov, *J. Chem. Phys.* **141**, 18C522 (2014).
- 51D. E. Dudalov, Y. D. Fomin, E. N. Tsiok, and V. N. Ryzhov, *Soft Matter* **10**, 4966 (2014).
- 52V. N. Ryzhov, E. E. Tareyeva, Y. D. Fomin, and E. N. Tsiok, *Phys. Usp.* **60**, 857 (2017).
- 53N. P. Kryuchkov, S. O. Yurchenko, Y. D. Fomin, E. N. Tsiok, and V. N. Ryzhov, *Soft Matter* **14**, 2152 (2018).

- <sup>54</sup>J. R. Bordin and L. B. Krott, *Phys. Chem. Chem. Phys.* **16**, 28740 (2016).
- <sup>55</sup>E. Salcedo, N. M. Barraz, and M. C. Barbosa, *J. Chem. Phys.* **138**, 164502 (2013).
- <sup>56</sup>P. Vilaseca and G. Franzese, *J. Chem. Phys.* **133**, 084507 (2010).
- <sup>57</sup>G. M. Viswanathan, E. P. Raposo, and M. G. E. da Luz, *Perspectives and Challenges in Statistical Physics and Complex Systems for the Next Decade* (World Scientific, 2014).
- <sup>58</sup>M. Szortyka, M. Girardi, V. Henriques, and M. C. Barbosa, *J. Chem. Phys.* **130**, 184902 (2009).
- <sup>59</sup>J. R. Bordin and L. B. Krott, *J. Phys. Chem. B* **121**, 4308–4317 (2017).
- <sup>60</sup>S. Prestipino, F. Saija, and P. V. Giaquinta, *J. Chem. Phys.* **133**, 144504 (2010).
- <sup>61</sup>S. Prestipino, F. Saija, and P. V. Giaquinta, *Phys. Rev. Lett.* **106**, 235701 (2011).
- <sup>62</sup>G. Malescio and G. Pellicane, *Nat. Mater.* **2**, 97 (2003).
- <sup>63</sup>G. Malescio and G. Pellicane, *Phys. Rev. E* **70**, 021202 (2004).